Energy Storage Materials xxx (xxxx) xxx

Contents lists available at ScienceDirect

Energy Storage Materials

journal homepage: www.elsevier.com/locate/ensm

Nanosheet-assembled hierarchical $Li_4Ti_5O_{12}$ microspheres for high-volumetric-density and high-rate Li-ion battery anode

Dongdong Wang [a,b], Haodong Liu [b], Mingqian Li [b], Xuefeng Wang [b], Shuang Bai [b], Yang Shi [b], Jianhua Tian [a], Zhongqiang Shan [a,**], Ying Shirley Meng [b,d], Ping Liu [b,d], Zheng Chen [b,c,d,*]

[a] School of Chemical Engineering and Technology, Tianjin University, Tianjin, 300350, PR China
[b] Department of NanoEngineering, Program of Chemical Engineering, University of California San Diego, La Jolla, CA, 92093, United States
[c] Program of Chemical Engineering, University of California San Diego, La Jolla, CA, 92093 United States
[d] Sustainable Power and Energy Center, University of California San Diego, La Jolla, CA, 92093, United States

ARTICLE INFO

Keywords:
$Li_4Ti_5O_{12}$
High tap density
High rate
$LiNi_{0.5}Mn_{1.5}O_4$ cathode
Full cell

ABSTRACT

Fast-charging (high-rate) is a critical need for lithium-ion batteries (LIBs). While superior rate performance can be achieved by nanostructured electrodes, their tap density is often low, which leads to low volumetric energy density and limits their practical applications. Here, we report nanosheet-assembled $Li_4Ti_5O_{12}$ (LTO) hierarchical microspheres which can simultaneously achieve high tap density, high rate performance and long cycle life. These microspheres were prepared with high yield by facile solvothermal reaction followed by a short thermal annealing process. The formation mechanism of such LTO microspheres was systematically investigated to understand their morphology evolution and phase transformation process. These well-designed hierarchical microspheres with controlled features on both nanometer- and micrometer-scales enable dense particle packing, easy lithium-ion diffusion and high structure robustness. Optimal LTO microspheres can offer extremely high rate capability (e.g., 155 mAh g^{-1} at 50 C), and excellent cycling stability (99.5% capacity retention after 2000 cycles at 50 C, 95.4% capacity retention after 3000 cycles at 30 C) with a tap density of 1.32 g cm^{-3}. Furthermore, their superior performance was also demonstrated with $LiNi_{0.5}Mn_{1.5}O_4$ cathode in full cells, which showed 93.4% of capacity retention after 1000 cycles at 3C. These results suggest the great promise of using such high-volumetric-density LTO as an anode material for high-rate and long-life LIBs.

1. Introduction

Lithium-ion batteries (LIBs) have widespread applications in portable electronics, electric vehicles (EVs) and grid energy storage [1–5]. Although commercial LIBs have been predominantly using graphite as the anode active material, they suffer from poor rate capability and safety issues [6–9]. In the recent years, spinel $Li_4Ti_5O_{12}$ (LTO) has attracted great attention as an alternative anode due to its superior safety feature since its lithium insertion/extraction voltage (1.55 V *vs.* Li^+/Li) is much higher than the potential needed for lithium deposition [10,11]. In addition, LTO exhibits negligible volume change during its discharge/charge process with high Li^+ insertion/extraction reversibility, which results in outstanding cycling stability [12–15]. However, its low electronic conductivity (10^{-13} S cm^{-1}) and small Li^+ diffusion coefficient (10^{-9}-10^{-13} cm^2 s^{-1}) restrict its potential application in high-power LIBs [16–18]. To increase the electronic and/or ionic conductivity, various strategies have been explored, including performing conductive coating and reducing the particle size by designing different nanostructures (nanoparticles, nanowires, nanotubes and nanosheets) [19–24]. Especially, LTO with nanosheet structures usually can show excellent rate performance owing to the shorter lithium ion diffusion paths [12,25,26]. While improved rate performance can be achieved by these approaches, these nanostructured LTO materials usually suffer from low tap density (<0.3–0.5 g cm^{-3}), which leads to low volumetric energy density and limits their practical applications [27–29]. In addition, nanosized LTO often forms severe aggregations during the charge/discharge process, which dramatically reduce their cycling stability [30].

Therefore, increasing the tap density of LTO anode materials (>1 g cm^{-3}) to obtain higher volumetric energy density is rather crucial for commercial applications. Compared to LTO with simple

* Corresponding author. Department of NanoEngineering, Program of Chemical Engineering, University of California San Diego, La Jolla, CA, 92093, United States.
** Corresponding author.
E-mail addresses: shanzq@tju.edu.cn (Z. Shan), zhengchen@eng.ucsd.edu (Z. Chen).

https://doi.org/10.1016/j.ensm.2019.05.036
Received 5 April 2019; Received in revised form 14 May 2019; Accepted 24 May 2019
Available online xxxx
2405-8297/

nanostructures, hierarchical architectures often possess higher tap density by combining nanostructured characteristics and micron-scale morphology. These features can provide nanoscale domain sizes for ion diffusion but still maintain effective particle packing to restrict self-aggregation during repeatedly charge/discharge process [31,32]. For example, Zhou et al. prepared LTO microspheres composed of nanosized particles with a tap density of 1.04 g cm^{-3} and a surface area of 30.8 $m^2 g^{-1}$. However, this LTO showed a specific capacity of only 86 and 73 mA h g^{-1} at 10 C and 20 C, respectively [33]. Lin et al. synthesized sub-micron mesoporous $Li_4Ti_5O_{12-x}$/C spheres with a tap density of 1.41 g cm^{-3} and surface area of 15.0 $m^2 g^{-1}$. They achieved a specific capacity of 119 mA h g^{-1} at 10 C after 100 cycles [34]. Although high tap densities have been achieved by forming these hierarchical LTO particles, their rate performance is still limited by their low surface area and inferior ion diffusion. In order to pursue higher rate capability, highly porous and hollow structured LTO microspheres with a large surface area were designed. For examples, Liu et al. prepared LTO hollow microspheres with high rate capability of 131.3 mA h g^{-1} at 20 C due to the large surface area of 107.04 $m^2 g^{-1}$ [35]. He et al. reported ultrathin LTO nanosheet-based hierarchical microspheres with a high specific surface area of 178 $m^2 g^{-1}$ and obtained a high capacity of 150 mA h g^{-1} at 50 C [36]. However, their highly porous and hollow structure can lead to low tap density (although specific value not mentioned). In addition, these low-density structures tend to easily breakdown during long-term battery cycling, leading to reduced capacity. Up to now, the development of LTO materials with high volumetric energy density, high rate performance, and long cycling stability remains a challenge.

Here, we show an effective design of hierarchical LTO architectures that can simultaneously achieve high tap density, high rate capability and ultrahigh stability. This is achieved by the successful synthesis of uniform LTO nanosheet-based hierarchical microspheres (U-LTO-NHMS) with high tap density (up to 1.32 g cm^{-3}) and moderate surface areas (from 51.91 to 67.03 $m^2 g^{-1}$). Their tap density can be controlled by regulating the size of microspherical secondary particles. The formation mechanism of U-LTO-NHMS was also systematically investigated by a series of precursor- and time-dependent experiments, which suggests that the growth of microspheres is typical Ostwald-ripening process. Owing to their uniformly hierarchical mesoporous micro-nanostructures, optimal U-LTO-NHMS showed nearly theoretical capacity, superior rate capability and ultrahigh cycling stability. Notably, after 2000 cycles at a high rate of 50 C, a specific capacity of 154.7 mA h g^{-1} is still maintained, corresponding to a capacity retention ratio of 99.5%. Moreover, we also demonstrated stable, high rate U-LTO-NHMS/$LiNi_{0.5}Mn_{1.5}O_4$ (LNMO) full cells with a capacity retention ratio of 93.4% after 1000 cycles at 3 C. These results indicate that U-LTO-NHMS can be an ideal anode material for high-rate and long-life LIBs.

2. Experimental section

2.1. Materials preparation

A solvothermal method was used to synthesize the U-LTO-NHMS samples. Two parts (A and B) of solution precursors were prepared. Solution A was obtained by dissolving 0.90 g of lithium hydroxide monohydrate ($LiOH·H_2O$) and cetyltrimethylammonium bromide (CTAB) in 30 mL of deionized (DI) water. Solution B was obtained by dispersing 1.0 mL of titanium butoxide in 30 mL of glycerol through stirring continuously. The solution A was added dropwise to solution B and the mixture was kept stirring for 8 h at 45 °C. The obtained transparent solution was transferred to a 100 mL Teflon-lined stainless autoclave and heated at 160 °C for 12 h. After cooling to room temperature naturally, samples were centrifuged, washed with anhydrous ethanol and deionized water repeatedly to remove organic residues and dried at 60 °C in a vacuum oven. Finally, the as-prepared precursors were calcined in a muffle furnace at 600 °C in air for 2 h to obtain the hierarchically nanostructured LTO samples, named as U-LTO-NHMS-160. By comparison, control samples were prepared by changing the solvothermal temperature to 180 and 200 °C with other conditions the same, the corresponding samples are named U-LTO-NHMS-180 and U-LTO-NHMS-200, respectively.

A hydroxide co-precipitation reaction, followed by high-temperature calcination was used for the synthesis of the ordered high voltage spinel LNMO. Transition metal (TM) nitrates, $Ni(NO_3)_2·6H_2O$ (ACROS Organics, 99%), and $Mn(NO_3)_2·4H_2O$ (Alfa Aesar, 98%), were dissolved in deionized water and then titrated into $LiOH·H_2O$ (Fisher) solution [37–39]. During the whole co-precipitation process, NH_4OH was used to control the pH value of the solution at 11.5. The precipitated TM hydroxides were then subjected to vacuum filtration and washed three times with deionized water. The collected TM hydroxides were dried in an oven at 180 °C for 10 h in air. The dried TM precursors were then mixed with a stoichiometric amount of $LiOH·H_2O$ (Fisher). This mixture was ground for 30 min to ensure adequate mixing and then placed into a furnace at 480 °C for 12 h [37–39]. Later, the pre-calcined powders were calcined at 900 °C for 16 h followed by a second calcination step at 700 °C for 8 h in air, to obtain the final product.

2.2. Materials characterization

The morphology of different samples was examined by Ultrahigh Resolution Scanning Electron Microscope (UHR-SEM, FEI XL30). Crystallographic structures of the samples were confirmed by X-ray diffraction (XRD) using Cu Kα radiation in the region of $2\theta = 10–80°$ at 30 kV and 10 mA (Bruker D2 Phaser, Germany). The phase purity was examined by Raman spectroscopy (DXR Microscope under a 532 nm, USA). Microstructural information and crystal characteristics of the samples were examined by Transmission Electron Microscopy (TEM, FEI Titan 80–300 kV S/TEM, America) images and selected area electron diffraction (SAED). Nitrogen adsorption and desorption isotherms were obtained using a QUADRASORB SI Quantachrome instrument (American) at 77 K with the specific surface area and pore size distribution determined by Brunauer-Emmett-Teller (BET) method and Barrett-Joyner-Halenda (BJH) model (desorption branch of the isotherms), respectively.

2.3. Electrochemical measurement

The electrodes were fabricated by casting the slurry of active materials (U-LTO-NHMS and $LiNi_{0.5}Mn_{1.5}O_4$), Super-P, and poly (vinylidene fluoride) (PVDF) binder with a mass ratio of 7:2:1 in N-methyl-2-pyrrolidone (NMP) solvent on Al or Cu foil, and then dried at 120 °C for 8 h in a vacuum oven before use [40]. Type CR-2032 coin cells were assembled to evaluate the electrochemical properties of all the samples. The electrolyte was 1 M $LiPF_6$ in a mixture of ethylene carbonate (EC)/diethyl carbonate (DEC) with a volume ratio of 1:1. Celgard 2400 microporous polypropylene membrane was used as the separator. For full cells, the mass loading of LTO was controlled at 3.0–3.5 mg cm^{-2}. The $LiNi_{0.5}Mn_{1.5}O_4$ (LNMO) was the capacity limiting electrode (N/P ratio was 1.1). Thus, the rate and specific capacity values of full cells were calculated based on the cathode mass. All cells were assembled in a glovebox filled with highly pure argon gas (O_2 and H_2O levels < 0.1 ppm). NEWARE battery testers were used to perform constant current charge-discharge cycling in the voltage range of 1.0–2.5 V and 1.7–3.4 V (*vs.* Li^+/Li). Cyclic voltammetry (CV) was measured using an Autolab electrochemical workstation between 1.0 and 2.5 V (*vs.* Li^+/Li) with different scan rates. Electrochemical impedance spectroscopy (EIS) measurements were executed by a Metrohm Autolab potentiostat in the frequency range with 0.1–10^5 Hz and a perturbation voltage of 5 mV.

3. Results and discussion

3.1. Physical characterization of materials

A typical synthesis of UM-LTONS samples mainly includes a

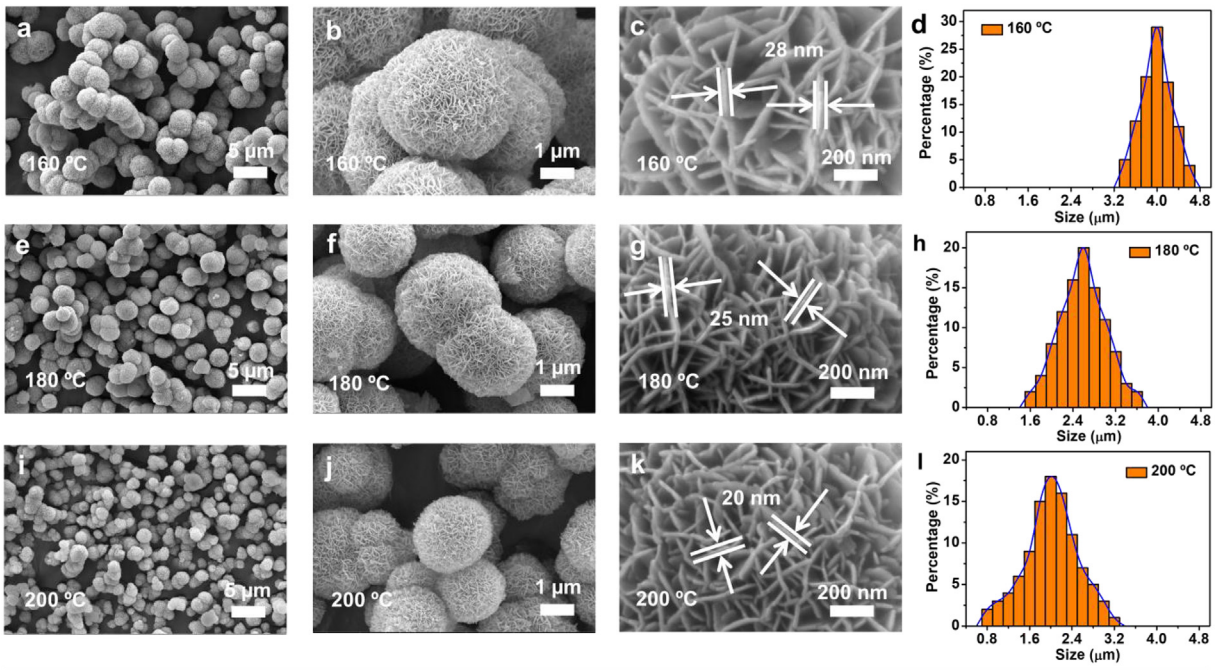

Samples	U-LTO-NHMS-160	U-LTO-NHMS-180	U-LTO-NHMS-200
Tap density (g cm^{-3})	1.32	1.14	1.01

Fig. 1. SEM images and size distribution plot of U-LTO-NHMS-160 (a, b, c, d), U-LTO-NHMS-180 (e, f, g, h), and U-LTO-NHMS-200 (i, j, k, l); the Table in the bottom is the summary of tap density of three samples.

controlled hydrolysis step followed by solvothermal reaction and then a short thermal annealing process. Initially, a transparent solution of titanium precursor was formed by dissolving titanium butoxide in glycerol. Rapid hydrolysis of titanium butoxide was prohibited at room temperature due to the capping effect of glycerol. Experiments also showed that the lithium source and the titanium precursor can readily form a homogenous solution in water/glycerol mixture at 45 °C. The reaction of lithium sources with the titanium precursor in the mild solvothermal process leads to the formation of microspherical Li–Ti–O precursor as the precipitate. Microspheres with different sizes can be obtained by varying the solvothermal reaction temperature (160, 180 and 200 °C). Hierarchical U-LTO-NHMS can be obtained after annealing the Li–Ti–O precursor at 600 °C in air. The resulted sample was denoted as U-LTO-NHMS-160, U-LTO-NHMS-180 and U-LTO-NHMS-200, respectively.

The morphology of the Li–Ti–O precursor and U-LTO-NHMS samples was first checked by scanning electron microscopic (SEM). As shown in Fig. S1, all the Li–Ti–O precursors have monodisperse and uniform hierarchical microspheres consisted of small nanosheets. For microspherical Li–Ti–O precursor particles obtained from the solvothermal reaction at different temperatures, their average diameter was found to be 4 ± 0.6, 2.6 ± 1.0 and 2 ± 1.2 μm for 160, 180 and 200 °C, respectively. Through magnified SEM images, the average thickness of nanosheets was identified to be 27, 24 and 18 nm for 160, 180 and 200 °C, separately (Fig. S 1c, g and k). Noted that there was no precipitation formed at lower solvothermal temperature (<160 °C), indicating that the hydrolysis of titanium butoxide in glycerol is temperature sensitive. After thermal annealing, all U-LTO-NHMS samples maintained the size and morphology of their Li–Ti–O precursors (Fig. 1a, e and i). It can be found that U-LTO-NHMS-160 has the most regular morphology among the three products due to a moderate solvothermal reaction temperature. For U-LTO-NHMS-180 and U-LTO-NHMS-200, some aggregation and broken microspheres are formed, possibly due to faster growth at higher solvothermal temperatures. SEM images with higher magnification (Fig. 1b, f and j) further reveal that each U-LTO-NHMS is constructed by many interconnected nanosheets. The average thickness of LTO nanosheets is 28, 25 and 20 nm, respectively (Fig. 1c, g and 1 k). In addition, Fig. 1d, h and l show that U-LTO-NHMS-160 has more uniform size distribution. The tap density of all U-LTO-NHMS is summarized in the Table of Fig. 1. Since U-LTO-NHMS-160 has the largest secondary particle size, it exhibits the highest tap density (1.32 g cm^{-3}) among the three samples. Such tap density also represents one of the highest values in literature (Table S1).

To investigate the microstructure evolution of LTO during the synthesis process, more detailed characterization was performed using U-LTO-NHMS-160 as an example. Transmission electron microscopic (TEM) images (Fig. 2a and b) clearly show the U-LTO-NHMS-160 precursors have microsphere structures consisted of uniform nanosheets. High-resolution TEM (HR-TEM) image (Fig. 2c) further shows the lattice spacing of 0.31 nm, which can be assigned to (310) plane of $Li_{1.81}H_{0.19}Ti_2O_5{\cdot}2H_2O$ [41]. After annealing, the microspherical morphology remained the same. Fig. 2d and e indicate that U-LTO-NHMS-160 maintained the microsphere structures constructed of thin nanosheets, which is consistent with the SEM results. Clear lattice fringes with an interplanar distance of 0.48 nm are observed, which agrees well with the (111) plane of spinel $Li_4Ti_5O_{12}$ (Fig. 2f). The selected area electron diffraction (SAED) pattern (Fig. 2f, inset) indicates that U-LTO-NHMS-160 is polycrystalline and these diffraction rings can be assigned to the (111), (311) and (400) planes of spinel $Li_4Ti_5O_{12}$ [42].

From the x-ray diffraction patterns (Fig. 3a), it can be identified that the crystal structure of all the samples match perfectly with the cubic spinel structure of $Li_4Ti_5O_{12}$ (JCPDS NO.49–0207, space group: $Fd\bar{3}m$) and no side peaks can be observed over the entire pattern, manifesting the high purity and high crystallinity of the final products. Raman spectra were measured to further confirm the structural characteristics of all the LTO samples. As shown in Fig. 3b, there are main characteristic peaks in the wavenumbers of 200–1000 cm^{-1}, which are assigned to F_{2g} (230 and

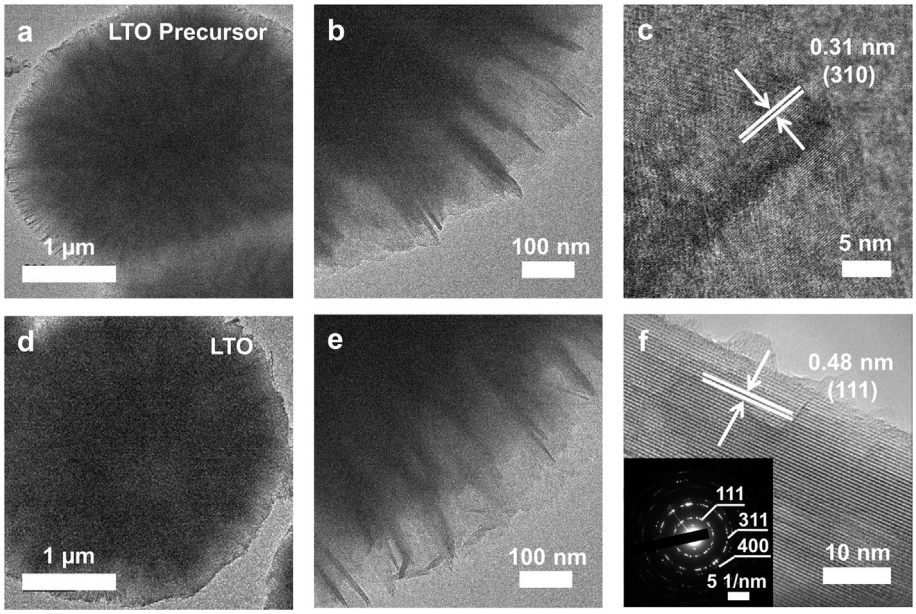

Fig. 2. TEM image (a) and HRTEM image (b) and (c) of the U-LTO-NHMS precursor; TEM image (d) and HRTEM image (e) and (f) of the U-LTO-NHMS-160 (the inset in (f) shows the relevant SEAD pattern).

347), E_g (420) and A_{1g} (670 and 740) modes of the spinel LTO, respectively [43]. More specifically, the lower frequency band at 230 cm^{-1} corresponds to the bending vibrations of O–Ti–O bonds and the bands at 347 cm^{-1} and 417 cm^{-1} are attributed to the stretching-bending vibrations of the Li–O bonds in LiO_6 and LiO_4 polyhedra, respectively. The higher frequency lines at 670 and 740 cm^{-1} should be ascribed to vibrations of Ti–O bonds in TiO_6 octahedra [44].

The surface area and pore structures of all the LTO samples were further characterized by nitrogen adsorption/desorption isotherms. The multi-point Brunauer-Emmett-Teller (BET) method was employed to compute the specific surface area. The pore size distribution was determined by using the Barrett-Joyner-Halenda (BJH) model based on the desorption curve of the isotherm. As displayed in Fig. 3c, all isotherms show a typical type IV curve with an H3 hysteresis, which suggests the presence of mesoporous structure and is in good agreement with the secondary sheet-like structures of hierarchical microspheres shown in SEM and TEM images. The corresponding pore size distributions of all samples confirm that the average pore size is about 20 nm, further suggesting that there is a uniform mesoporous structure (Fig. 3d). The specific surface areas and pore volumes of all samples are compared in Table S2. Although three samples all show moderate specific surface areas and pore volumes, U-LTO-NHMS-160 reveal a slightly larger BET surface area (67.03 $m^2 g^{-1}$) and a larger pore volume (0.54 $cm^3 g^{-1}$) among the three samples, which can be ascribed to the more regular nanosheet-assemble morphology and uniform size.

3.2. Formation mechanism of the LTO microspheres

In order to study the formation mechanism of U-LTO-NHMS with more details, a series of time-dependent solvothermal experiments were carried out. The morphological evolutions of U-LTO-NHMS precursors under different solvothermal time were examined by TEM and SEM (Fig. 4). In the initial stage of solvothermal reactions (1 h), only colloidal suspension can be obtained and no solid precipitation was formed. The suspension was directly loaded onto a copper grid. TEM image (Fig. 4a) shows that the products are well-dispersed nanosheets mainly in a hexagonal shape with a size range from 50 nm to 100 nm. When the reaction time increasing to 2 h, the colloidal suspension becomes more viscous and the nanosheets fuse together and transform into clusters (Fig. 4b). There is still no solid product, possibly owing to the prohibition of nucleation growth by glycerol [45]. As the reaction time increases to 3 h, white solids begin to precipitate from the suspension. The SEM image (Fig. 4c) shows that a large number of microspheres with a rough surface are generated. With further increase of the solvothermal time (4 h), nanosheets start to emerge on the surface of the microspheres (Fig. 4d). Interestingly, each microsphere presents a deep hole, which can be associated with a typical Ostwald-ripening process [46]. Consistently, as the reaction continuously proceeds (6 and 8 h), the size and depth of the holes decrease until they disappear (Fig. 4e and f). When the reaction time reaches 12 h, complete hierarchical microspheres built by interconnected regular nanosheets are formed (Fig. 4g). Their morphology maintains nearly the same (Fig. 4h) even though reaction time is further increased to 24 h.

On the other hand, the evolution of the crystal structure of the L-Ti-O precursor microspheres under different solvothermal time was investigated by XRD measurement. As shown in Fig. 5a, when the solvothermal reaction time was prolonged to 3 h, the reactants can be transformed into the layered $Li_{1.81}H_{0.19}Ti_2O_5{\cdot}2H_2O$ without phase impurities [25]. Additionally, as the reaction time increases, the $Li_{1.81}H_{0.19}Ti_2O_5{\cdot}2H_2O$ phase shows increased crystallinity. The precursor obtained at each stage of hydrothermal reaction was subject to thermally annealing to complete phase transformation. Fig. 5b shows that the layered structure precursor can be successfully converted into spinel $Li_4Ti_5O_{12}$. For precursor particles prepared with solvothermal reaction time below 6 h, anatase TiO_2 phase can be identified, which may be ascribed to insufficient lithiation of titanium moieties. When the reaction proceeds to 8 and 12 h, pure phase LTO can be obtained, suggesting adequate lithiation during the solvothermal reaction step. However, further increasing the reaction time to 24 h, results in the formation of Li_2TiO_3 phase, owing to over-lithiation of the titanium moieties.

In the glycerol/water system, water can accelerate the hydrolysis reaction. The linkages between nuclei containing titanium atoms and glycerol skeletons can be formed, which makes the liquid solutions highly viscous [47]. As a result, the diffusion of the TiO_2 nuclei will be difficult, and the aggregation of these TiO_2 nuclei into larger grains may be remarkably decreased, which greatly limits the condensation process [47]. In addition, an earlier study has shown that hydrolysis is fast and the condensation is a slow step in the synthesis of TiO_2 powders by hydrolysis of titanium tetraethoxide. Therefore, the overall reaction may reach an equilibrium state depending on glycerol/water volume ratio

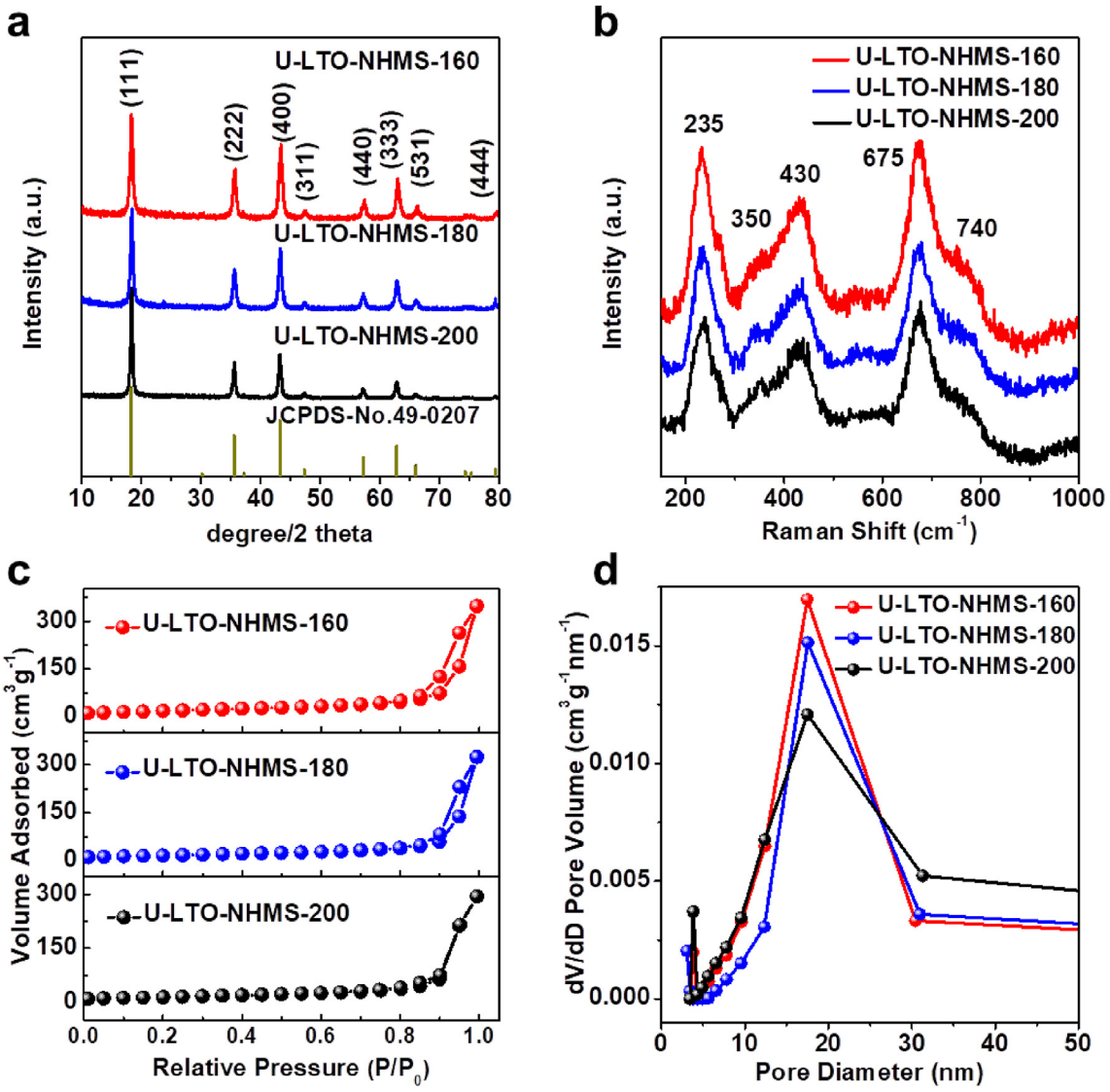

Fig. 3. XRD patterns (a), Raman spectra (b), nitrogen adsorption-desorption isotherms (c) and pore size distributions (d) of the three LTO samples synthesized at different solvothermal temperatures (160, 180 and 200 °C).

[48]. In this work, we also carefully examined this effect. It was found that when the volume ratio between glycerol and water (V_{water}:$V_{glycerol}$) was adjusted in the range from 10:50 to 25:35, no solid precipitate can be formed, possibly due to the inhibition of condensation by high concentration of glycerol. On the other hand, when increasing the amount of water to reach V_{water}:$V_{glycerol}$ of 40:20, the size of the microspheres become nonuniform and some aggregation occurs because of more rapid hydrolysis reactions (Fig. S2a). With further increase of the amount of water (V_{water}:$V_{glycerol}$ = 50:10), the aggregation becomes more random and the microsphere morphology cannot be maintained (Fig. S2b). When even more water was used (V_{water}:$V_{glycerol}$ = 55:5), no microspheres can be formed and only aggregated nanoparticles were produced (Fig. S2c). Therefore, V_{water}:$V_{glycerol}$ of 30:30 was found to be an optimal volume ratio to allow the formation of uniformly hierarchical microspheres.

The concentration of CTAB surfactant in the precursor solutions can also affect the morphology of the L-T-O microsphere precursor. In order to exam its factors, a series of experiments with different CTAB concentrations were performed. The duration of the solvothermal reaction was controlled to be 12 h. Without adding CTAB (Fig. S3a), microspheres can be produced but their size is not uniform. In addition, the surface of the microspheres is smooth, suggesting that no nanosheets are formed. When the 0.01 M CTAB is added, the porous surface can be observed on each microsphere, although their size remains non-uniform (Fig. S3b). As the concentration increased to 0.02 M, size-uniform microspheres (with a rough surface) composed of nanosheets can be obtained (Fig. S3c). With further increase of the CTAB concentration to 0.05 M, holes start to emerge in the microspheres (Fig. S3d). It was found that the size of each hole in microspheres become larger when the concentration of CTAB continuously increased to 0.1 M (Fig. S3e). At the same time, as shown in Fig. S3f, the yield of microspheres decreased from 90.4% to 15.4% as the CTAB concentration increases from 0 to 0.1 M. These results suggest that the presence of CTAB inhibits the Ostwald-ripping process of the dissolved precursor molecules. This is likely due to the fact that the linkages between TiO_2 nuclei and CTAB chains can prevent the condensation of TiO_2 nuclei as well as the following growth process [49].

In view of the above experiments results, the formation mechanism of U-LTO-NHMS can be illustrated in Fig. 6. At the initial stage of solvothermal reaction in an optimal precursor solution, colloidal nanoparticles are generated due to fast hydrolysis and nuclei growth in the alkaline environment. As the reaction proceeds, porous microspheres with a rough surface were formed due to typical Ostwald-ripening mechanism. Continuous dissolution and recrystallization lead to uniform microspheres constructed by small nanosheets. At the same time, solvothermal lithiation of Ti moieties with Li sources results in layered

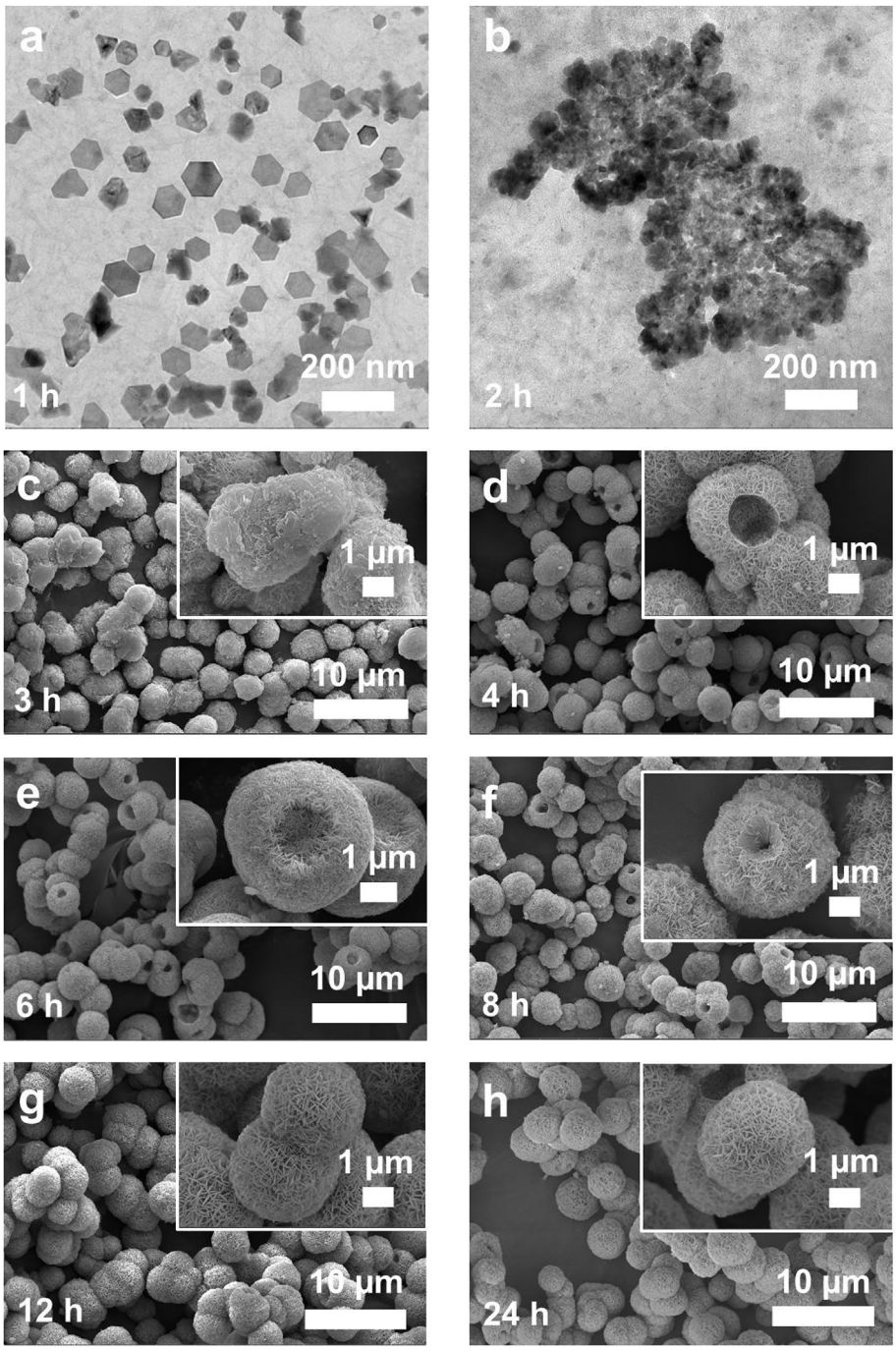

Fig. 4. TEM images and SEM images showing the morphological evolution of the obtained U-LTO-NHMS precursors prepared with different solvothermal time: (a) 1 h, (b) 2 h, (c) 3 h, (d) 4 h, (e) 6 h, (f) 8 h, (g) 12 h, (h) 24 h.

$Li_{1.81}H_{0.19}Ti_2O_5{\cdot}2H_2O$. Layered-to-spinel phase transformation occurs by thermal annealing in air, and the hierarchical microspheres with uniform size and morphology are obtained.

3.3. Electrochemical performance

The electrochemical properties of U-LTO-NHMS samples were evaluated as anodes for LIBs. Galvanostatic discharge-charge voltage profiles of the three electrodes operated at different rates from 1 to 50 C in the voltage range of 1.0–2.5 V (*vs.* Li^+/Li) are shown in Fig. 7a and Figs. S4a and b. A very flat plateau with two sloping regions (at 2.5–1.5 V and 1.5–1.0 V vs Li^+/Li) was observed in all three samples. The flat plateau at about 1.55 V contributes to the majority of the total capacity, showing the inherent feature of a two-phase reaction based on the Ti^{4+}/Ti^{3+} redox couple [50]. At the low current rate of 1 C, the three electrodes all deliver a stable specific capacity of about 175.0 mAh g^{-1}, which is close to the theoretical capacity of LTO [51]. As the rate increases, the potential plateau becomes shorter and gradually distorts, suggesting that the polarization augments with the increasing rate, which is a common behavior of battery electrodes [52–54].

One advantage of LTO compared with graphite anode is its high rate capability. Fig. 7b shows the rate performance of the three U-LTO-NHMS electrodes at different rates of 1–50C in voltage range of 1.0–2.5 V. Although all the electrodes showed high initial capacity and good rate capability, U-LTO-NHMS-160 shows the highest discharge capacity than the other two samples, especially at high current rates (Table S3), owing

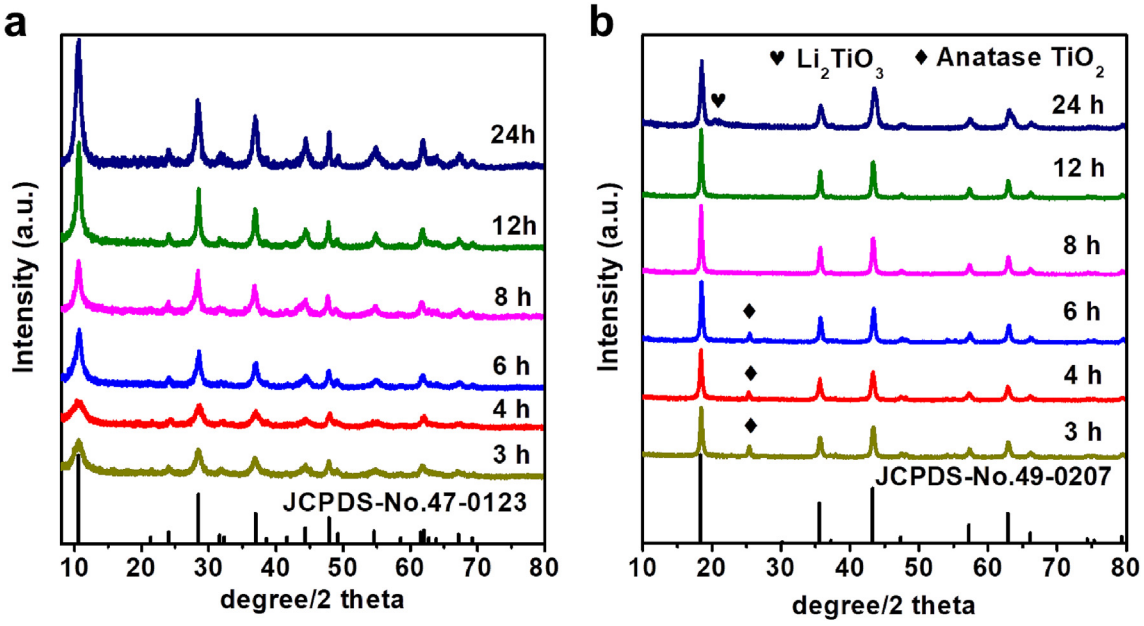

Fig. 5. XRD patterns of (a) U-LTO-NHMS precursors and (b) U-LTO-NHMS with different solvothermal times.

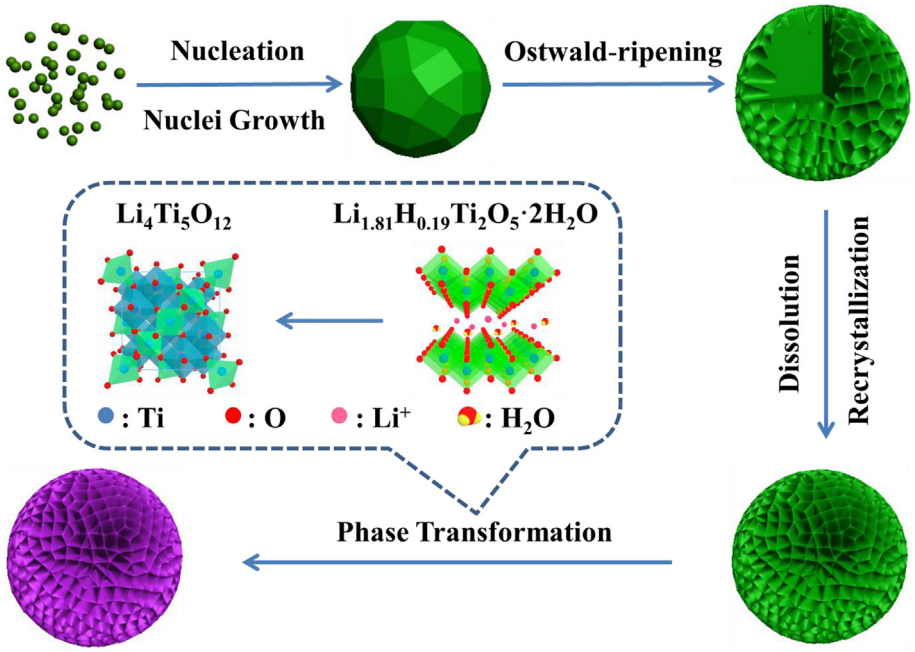

Fig. 6. Illustration of the formation mechanism of the hierarchical U-LTO-NHMS microspheres from Ostwald-ripening to phase transformation.

to the largest specific surface areas and regular mesoporous structures. The average discharging capacities are 175, 173, 169, 166, 162, 160 mAh g^{-1} at rates of 1, 2, 5, 10, 20, 30 C, respectively. Even at a high rate of 50 C, a discharge capacity of 155 mAh g^{-1} can be still retained. After cycling at 50 C, the discharge capacity recovers to 175 mAh g^{-1} with nearly 100% capacity retention once the current rate is reversed back to 1 C, highlighting the high resilience and good structural robustness of the U-LTO-NHMS-160 electrodes.

As mentioned earlier, although several high-rate LTO electrodes have been reported before, achieving high volumetric density at the same time remains a challenging task. Fig. 7c summarizes the volumetric capacity under different current rates of reported LTO materials with a high tap density (>1 g cm^{-3}) [8,31,33,34,55–59]. It is found that U-LTO-NHMS-160 shows the largest volume capacity under high current rate (>10 C).

Besides the excellent rate capability, U-LTO-NHMS-160 also displays outstanding cycling performance. The three LTO electrodes all show stable cycling performance after 500 cycles at a low rate of 1 C with almost no capacity decay and average coulombic efficiency of 99.99% (Fig. 7d, Figs. S4c and 4d). Meanwhile, the long-term cycling stability of three electrodes at a high rate of 50 C is also compared. As shown in Fig. 7e, for U-LTO-NHMS-160 electrode, a specific capacity of 154.7 mAh g^{-1} was still obtained after 2000 cycles with a capacity retention of 99.5%. However, for U-LTO-NHMS-180 and U-LTO-NHMS-200, the capacity retention was only 89.8% and 86.2% after 2000 cycles, respectively. In addition, 95.4% capacity retention was also achieved for U-

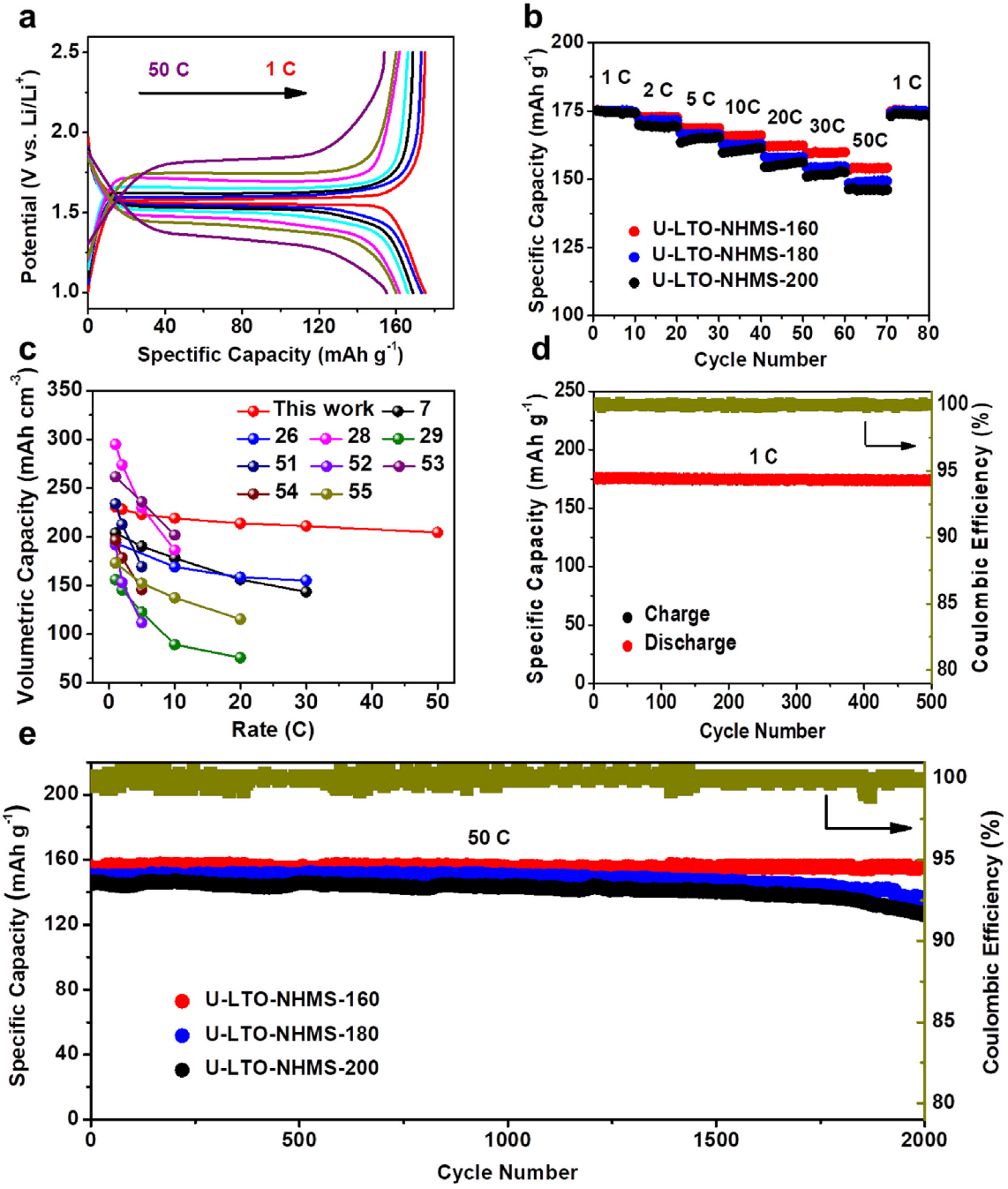

Fig. 7. (a) Galvanostatic discharging/charging voltage profiles of the U-LTO-NHMS-160 at different current rates of 1, 2, 5, 10, 20, 30 and 50 C; (b) Rate performance of the three samples (U-LTO-NHMS-160, U-LTO-NHMS-180 and U-LTO-NHMS-200); (c) Cycling performance of the U-LTO-NHMS-160 at rate of 1 C; (d) Cycle performance of the three UM-LTONS samples at high rate of 50 C (1C = 175 mA g^{-1}).

LTO-NHMS-160 at a high rate of 30 C (Fig. S5). To our best knowledge, such outstanding high-rate cycle performance is superior to any other reported LTO anode materials in the literature (Table S4). In order to further evaluate the structural stability of the three electrodes, cycled cells were disassembled in an Ar-filled glove box, and the morphology of the cycled U-LTO-NHMS electrodes after 2000 cycles at a high current rate of 50 C was compared (Fig. S6). Compared with electrodes before and after cycling, it is found that U-LTO-NHMS-160 still maintained the hierarchical microspherical structure composed by nanosheets while some aggregation and/or pulverization occur in U-LTO-NHMS-180 and U-LTO-NHMS-200 electrodes. Therefore, the outstanding cycling stability of U-LTO-NHMS-160 electrodes can be attributed to their structural stability originated from robust hierarchical microsphere structures.

To analyze the electrochemical properties of the three U-LTO-NHMS electrodes, cyclic voltammetry (CV) measurement were carried out at different scan rates from 0.1 to 10 mV s^{-1}. As shown in Fig. 8a, Figs. S7a and S7b, the three electrodes all show a pair of typical anodic and cathodic peaks at nearly 1.55 V at a low scan rate of 0.1 mV s^{-1}, which is associated with the two-phase redox reaction mechanism of $Li_4Ti_5O_{12}$ ($Li_4Ti_5O_{12} + 3Li^+ + 3e^- \leftrightarrow Li_7Ti_5O_{12}$) [60]. The relationship between peak current i and scan rate v follows the power law $i = a^*v^b$, where a and b are adjustable values (If $b = 1$, the total capacity comes from the interfacial Li storage process; if $b = 0.5$, it is diffusion-controlled Li^+ insertion-extraction process) [51,61]. It can be found that the relationship of log (v) and log (i) for all three electrodes is close to a linear relationship (Fig. 8b, Figs. S7c and S7d). For example, the fitted b values

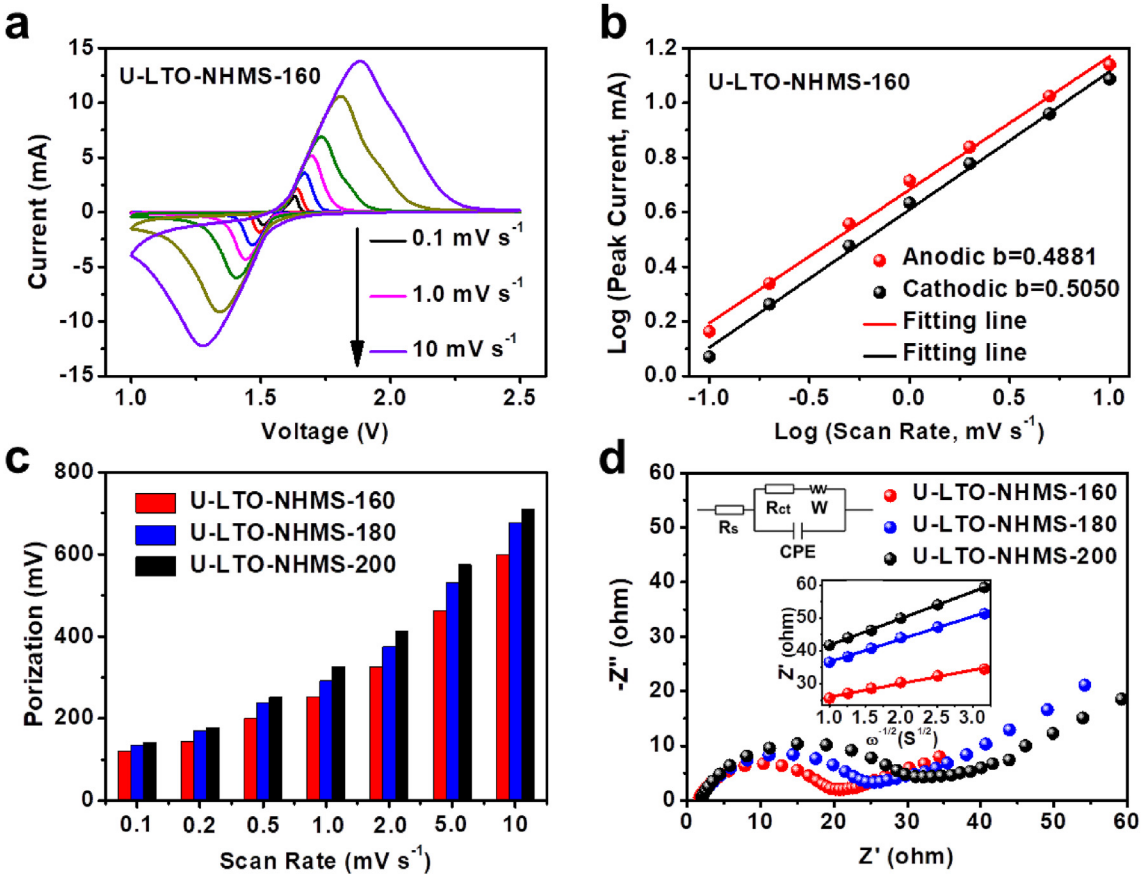

Fig. 8. (a) CV curves of U-LTO-NHMS-160 at different scan rates of 0.1, 0.2, 0.5, 1.0, 2.0, 5.0 and 10 mV s^{-1}; (b) Corresponding log (scan rate)-log (peak current) profiles of U-LTO-NHMS-160 at different scan rates of 0.1, 0.2, 0.5, 1.0, 2.0, 5.0 and 10 mV s^{-1}; (c) the relationship of scan rates and voltage separation of cathodic and anodic peak; (d) EIS spectra of three U-LTO-NHMS samples; the inset of (d) is the equivalent circuit model and plot of Z' versus $\omega^{1/2}$ of three U-LTO-NHMS samples in the low-frequency region.

of the cathodic and anodic peak currents on the CV for U-LTO-NHMS-160 electrode are 0.51 and 0.49, respectively. In spite of their relatively large surface area, these results confirm that the lithiation/de-lithiation of the three electrodes is mainly based on a diffusion-controlled process rather than the surface reaction. In addition, with the increase of scan rates, the U-LTO-NHMS-160 electrodes exhibit the smallest voltage gap (ΔE_p) between the cathodic and anodic peaks, suggesting the smallest polarization (Fig. 8c).

The superior electrochemical performance of U-LTO-NHMS-160 electrodes among the three electrodes was further supported by EIS measurement (Fig. 8d). The impedance spectra were fitted with the modified Randle-Ershler equivalent circuit model (inset of Fig. 8d). The intersection of the Nyquist plot with the Z' axis known as the ohmic resistance (R_s) shows the contribution from the internal resistance of electrode and electrolyte in LIBs. The charge-transfer impedance (R_{ct}) is expressed by the depressed semicircle in the intermediate frequency region. Warburg impedance (W), which is also known as the solid-state diffusion resistance, can be reflected in the slope line at low frequencies. The constant phase elements (CPE) are used to represent the double-layer capacitance [62,63]. All the fitting results are listed in Table S6. The UM-LTONS-600 electrode shows the smallest R_s and R_{ct} among the three electrodes. Furthermore, Li^+ diffusion coefficient (D_{Li+}) can also be calculated from the following equation (1) [64,65].

$$D_{Li} = \frac{R^2T^2}{2A^2n^4F^4C^2\sigma^2} \quad (1)$$

Where R is the gas constant (8.314 J K^{-1} mol^{-1}), T is the absolute temperature (298 K), A is the surface area of electrode, n is the number of electrons transferred in the half-reaction for the redox reaction, F is the Faraday constant (96500 C mol^{-1}), C is the concentration of lithium ions, σ is the Warburg factor, which is based on Equation (2), and can be obtained from the slope of $Z' \sim \omega^{-1/2}$ plot as depicted in Fig. 8d (inset).

$$Z' = R_b + R_{sei} + R_{ct} + \sigma\omega^{-1/2} \quad (2)$$

The calculated D_{Li+} values of the three electrodes are shown in Table S5. U-LTO-NHMS-160 displays the largest D_{Li+} (1.89×10^{-11}), which is about 3 and 4 times larger than that of U-LTO-NHMS-180 and U-LTO-NHMS-200. These results are consistent with its highest rate performance of the U-LTO-NHMS-160 electrodes.

To further demonstrate the potential application of the U-LTO-NHMS-160 anode, full cells were assembled and tested with high-voltage LNMO as the cathode. Detailed synthesis, structure and morphology characterization were reported in previous work [66]. Briefly, the XRD pattern confirms that cathode materials show a cubic spinel structure of LNMO with high purity (Fig. S8a). The LNMO particles presenthierarchical microsphere morphology consisted of rectangular micro-rods (Fig. S8b). Half-cell test shows that the LNMO cathode displays a high voltage plateau at about 4.7 V, and can deliver a specific capacity of 148.3, 133.6, 118.3, 88.6 and 44 mAh g^{-1} at different rates of 0.5, 1, 2, 5 and 10 C, respectively (Fig. S8c). In addition, the electrode shows little capacity decay after 200 cycles at 1 C (Fig. S8d).

The CV curves of LTO-LNMO full cells in the first three cycles at a scan rate of 0.1 mV s^{-1} were measured. As shown in Fig. 9a, all curves have two redox peaks in the region of 3.1–3.2 V and a very small peak around 2.6 V, which attributes to the Ni^{2+}/Ni^{4+} redox and Mn^{3+}/Mn^{4+} redox reaction, respectively [66]. Fig. 9b shows typical voltage profiles of the

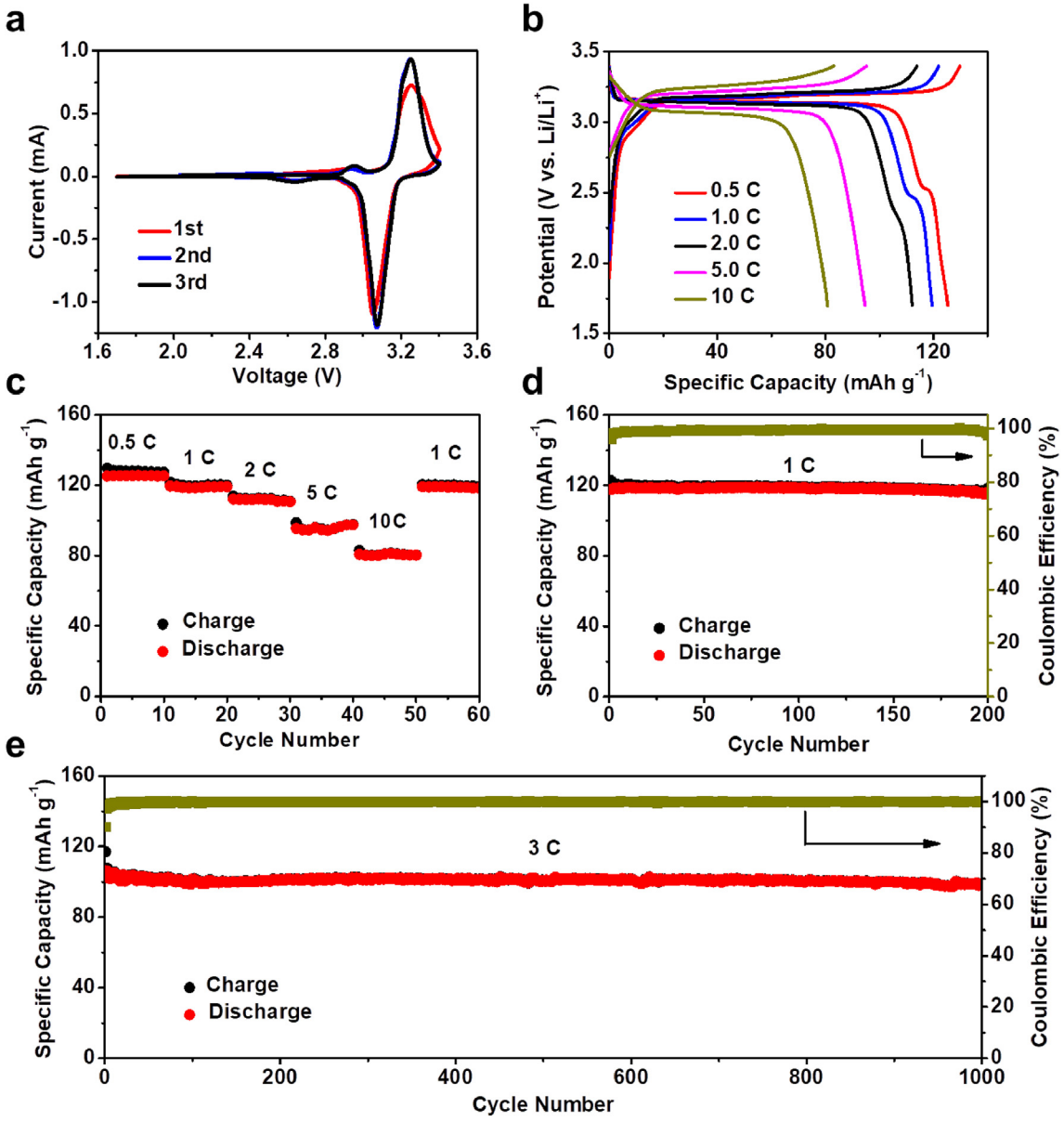

Fig. 9. Electrochemical performance of the LTO/LNMO full cell: (a) CV curves of initial three cycles at scan rates of 0.1 mV s^{-1}; (b) Galvanostatic discharging/charging voltage profiles at different current rates of 0.5, 1, 2, 5 and 10 C; (c) Rate performance at different current rates of 0.5, 1, 2, 5 and 10 C; Cycling performance and coulombic efficiency at (d) 1 C and (e) 3C (1C = 147 mA g^{-1}).

charge-discharge cycles of the LTO-LNMO full cells at different rates. Noted that the high voltage plateau at 3.1–3.2 V and the low voltage plateau at ~2.6 V is obtained, which is in agreement with the CV results. Although the rate capability of the full cell is limited by LNMO cathode, the full cell can deliver specific capacities of 126, 120, 112, 95, and 81 mAh g^{-1} at 0.5,1, 2, 5 and 10 C, respectively (based on cathode mass), indicating excellent rate performance (Fig. 9c). Furthermore, the full cell also exhibits remarkable cycling stability with almost no capacity loss after 200 cycles at 1 C (Fig. 9d). Notably, as further shown in Fig. 9e, after 1000 cycles at 3 C, the full cell can still maintain 93.4% of the initial capacity with average Coulombic efficiency of 99.92%. Such stable cycling performance of the LTO/LNMO full cell shows superior advantages over other reported works (Table S6). The excellent electrochemical performance can be attributed to the effective integration of the hierarchical microsphere LTO anode and LNMO cathode, which not only provides high rate capability but also ensures stable cycling at various charge/discharge rates.

4. Conclusion

In summary, we have developed a simple method for synthesizing uniform $Li_4Ti_5O_{12}$ nanosheet-based hierarchical microspheres, which combines a facile solvothermal process and thermal annealing treatment. The microspheres possess a high tap density of up to 1.32 g cm^{-3}. The formation mechanism of U-LTO-NHMS has been systemically investigated which suggests that the water/alcohol ratio, concentration of surfactant and reaction time are key factors determining their morphology. Due to the nanosheet-assembled hierarchal structure, the LTO microspheres show high specific capacity, exceptionally high rate capability, and outstanding cycling stability. Particularly, the U-LTO-NHMS-160 delivers a specific capacity of 175 mAh g^{-1} at 1C, and still maintains a high capacity of 155 mAh g^{-1} at an ultra-high rate of 50 C (1.2 min charge time). At the same time, it shows almost no capacity fading (capacity retention of 99.5%) after 2000 cycles at 50 C. This high-rate and stable cycling properties of U-LTO-NHMS were also confirmed by U-LTO-NHMS/$LiNi_{0.5}Mn_{1.5}O_4$ full cell testing. As a result, the full cell

exhibits high capacity retention of 93.4% after 1000 cycles at 3 C. These results indicate that U-LTO-NHMS can be a promising anode material for high-rate and long-life LIBs with great promise for commercial applications.

Conflict of interest

The authors declare no competing financial interest.

Acknowledgements

Z. Chen acknowledges the start-up fund support from UC San Diego. The support provided by China Scholarship Council during a visit of D. D. Wang to University of California San Diego is acknowledged (No. 201706250088). Y. S. Meng and S. Bai thank the Sustainable Power and Energy Center (SPEC) at UC San Diego for partial support for this work. TEM work was performed at UC Irvine Materials Research Institute (IMRI). This work was performed in part at the San Diego Nanotechnology Infrastructure (SDNI) of UCSD, a member of the National Nanotechnology Coordinated Infrastructure, which is supported by the US National Science Foundation (grant ECCS-1542148).

Appendix A. Supplementary data

Supplementary data to this article can be found online at https://doi.org/10.1016/j.ensm.2019.05.036.

References

[1] M. Armand, J.-M. Tarascon, Nature 451 (2008) 652.
[2] Z.W. Seh, W. Li, J.J. Cha, G. Zheng, Y. Yang, M.T. McDowell, P.-C. Hsu, Y. Cui, Nat. Commun. 4 (2013) 1331.
[3] A. Manthiram, J.C. Knight, S.T. Myung, S.M. Oh, Y.K. Sun, Adv. Energy Mater. 6 (2016) 1501010.
[4] S. Hy, H. Liu, M. Zhang, D. Qian, B.-J. Hwang, Y.S. Meng, Energy Environ. Sci. 9 (2016) 1931–1954.
[5] Z. Yao, X. Xia, Y. Zhang, D. Xie, C. Ai, S. Lin, Y. Wang, S. Deng, S. Shen, X. Wang, Nanomater. Energy 54 (2018) 304–312.
[6] X. Huang, H. Yu, J. Chen, Z. Lu, R. Yazami, H.H. Hng, Adv. Mater. 26 (2014) 1296–1303.
[7] C. Wang, S. Wang, L. Tang, Y.-B. He, L. Gan, J. Li, H. Du, B. Li, Z. Lin, F. Kang, Nanomater. Energy 21 (2016) 133–144.
[8] C. Wang, S. Wang, Y.-B. He, L. Tang, C. Han, C. Yang, M. Wagemaker, B. Li, Q.-H. Yang, J.-K. Kim, Chem. Mater. 27 (2015) 5647–5656.
[9] M.D. Radin, S. Hy, M. Sina, C. Fang, H. Liu, J. Vinckeviciute, M. Zhang, M.S. Whittingham, Y.S. Meng, A. Van der Ven, Adv. Energy Mater. 7 (2017) 1602888.
[10] C.a. Zhou, X. Xia, Y. Wang, Z. Yao, J. Wu, X. Wang, J. Tu, Small 14 (2018) 1704339.
[11] Z. Yao, X. Xia, D. Xie, Y. Wang, C.a. Zhou, S. Liu, S. Deng, X. Wang, J. Tu, Adv. Funct. Mater. 28 (2018) 1802756.
[12] Y.-Q. Wang, L. Gu, Y.-G. Guo, H. Li, X.-Q. He, S. Tsukimoto, Y. Ikuhara, L.-J. Wan, J. Am. Chem. Soc. 134 (2012) 7874–7879.
[13] J. Liu, K. Song, P.A. van Aken, J. Maier, Y. Yu, Nano Lett. 14 (2014) 2597–2603.
[14] S. Chen, Y. Xin, Y. Zhou, Y. Ma, H. Zhou, L. Qi, Energy Environ. Sci. 7 (2014) 1924–1930.
[15] Y. Ma, B. Ding, G. Ji, J.Y. Lee, ACS Nano 7 (2013) 10870–10878.
[16] X. Lu, L. Gu, Y.S. Hu, H.C. Chiu, H. Li, G.P. Demopoulos, L. Chen, J. Am. Chem. Soc. 137 (2015) 1581–1586.
[17] L. Shen, B. Ding, P. Nie, G. Cao, X. Zhang, Adv. Energy Mater. 3 (2013) 1484–1489.
[18] L. Sun, W. Kong, H. Wu, Y. Wu, D. Wang, F. Zhao, K. Jiang, Q. Li, J. Wang, S. Fan, Nanoscale 8 (2016) 617–625.
[19] K.-T. Kim, C.-Y. Yu, C.S. Yoon, S.-J. Kim, Y.-K. Sun, S.-T. Myung, Nanomater. Energy 12 (2015) 725–734.
[20] A.K. Haridas, C.S. Sharma, T.N. Rao, Small 11 (2015) 290–294.
[21] Q. Zhou, L. Liu, J. Tan, Z. Yan, Z. Huang, X. Wang, J. Power Sources 283 (2015) 243–250.
[22] T. Meng, R. Zeng, Z. Sun, F. Yi, D. Shu, K. Li, S. Li, F. Zhang, H. Cheng, C. He, J. Electrochem. Soc. 165 (2018) A1046–A1053.
[23] C. Chen, Y. Huang, C. An, H. Zhang, Y. Wang, L. Jiao, H. Yuan, ChemSusChem 8 (2015) 114–122.
[24] Q. Tian, P. Chen, Z. Zhang, L. Yang, J. Power Sources 350 (2017) 49–55.
[25] D. Wang, Z. Shan, J. Tian, Z. Chen, Nanoscale 11 (2019) 520–531.
[26] X. Feng, H. Zou, H. Xiang, X. Guo, T. Zhou, Y. Wu, W. Xu, P. Yan, C. Wang, J.-G. Zhang, ACS Appl. Mater. Interfaces 8 (2016) 16718–16726.
[27] M. Odziomek, F. Chaput, A. Rutkowska, K. Świerczek, D. Olszewska, M. Sitarz, F. Lerouge, S. Parola, Nat. Commun. 8 (2017) 15636.
[28] Y. Sha, X. Xu, L. Li, R. Cai, Z. Shao, J. Power Sources 314 (2016) 18–27.
[29] Y. Zhang, Y. Zhang, L. Huang, Z. Zhou, J. Wang, H. Liu, H. Wu, Electrochim. Acta 195 (2016) 124–133.
[30] D. Ruan, M.-S. Kim, B. Yang, J. Qin, K.-B. Kim, S.-H. Lee, Q. Liu, L. Tan, Z. Qiao, J. Power Sources 366 (2017) 200–206.
[31] L. Tang, Y.B. He, C. Wang, S. Wang, M. Wagemaker, B. Li, Q.H. Yang, F. Kang, Adv. Sci. 4 (2017) 1600311.
[32] D. Wang, G. Zhang, Z. Shan, T. Zhang, J. Tian, ChemElectroChem 5 (2018) 540–545.
[33] C. Dai, J. Ye, S. Zhao, P. He, H. Zhou, Chem. Asian J. 11 (2016) 1273–1280.
[34] C. Lin, M.O. Lai, H. Zhou, L. Lu, Phys. Chem. Chem. Phys. 16 (2014) 24874–24883.
[35] Q. Zhou, L. Liu, H. Guo, R. Xu, J. Tan, Z. Yan, Z. Huang, H. Shu, X. Yang, X. Wang, Electrochim. Acta 151 (2015) 502–509.
[36] Y. He, A. Muhetaer, J. Li, F. Wang, C. Liu, Q. Li, D. Xu, Adv. Energy Mater. 7 (2017) 1700950.
[37] H. Liu, D. Qian, M.G. Verde, M. Zhang, L. Baggetto, K. An, Y. Chen, K.J. Carroll, D. Lau, M. Chi, ACS Appl. Mater. Interfaces 7 (2015) 19189–19200.
[38] M.G. Verde, H. Liu, K.J. Carroll, L. Baggetto, G.M. Veith, Y.S. Meng, ACS Appl. Mater. Interfaces 6 (2014) 18868–18877.
[39] H. Liu, C.R. Fell, K. An, L. Cai, Y.S. Meng, J. Power Sources 240 (2013) 772–778.
[40] B.-S. Lee, Z. Wu, V. Petrova, X. Xing, H.-D. Lim, H. Liu, P. Liu, J. Electrochem. Soc. 165 (2018) A525–A533.
[41] K. Zhu, H. Gao, G. Hu, M. Liu, H. Wang, J. Power Sources 340 (2017) 263–272.
[42] D. Wang, Z. Shan, X. Liu, R. Na, J. Wang, H. Liu, J. Tian, Electrochim. Acta 262 (2018) 9–17.
[43] Y. Cai, Y. Huang, W. Jia, X. Wang, Y. Guo, D. Jia, Z. Sun, W. Pang, Z. Guo, J. Mater. Chem. 4 (2016) 9949–9957.
[44] I.A. Leonidov, O.N. Leonidova, L.A. Perelyaeva, R.F. Samigullina, S.A. Kovyazina, M.V. Patrakeev, Phys. Solid State 45 (2003) 2183–2188.
[45] Z. Zhang, C. Jiang, P. Du, Y. Wang, Ceram. Int. 41 (2015) 3932–3939.
[46] Z.-Q. Li, W.-C. Chen, F.-L. Guo, L.-E. Mo, L.-H. Hu, S.-Y. Dai, Sci. Rep. 5 (2015) 14178.
[47] T. Trung, W.-J. Cho, C.-S. Ha, Mater. Lett. 57 (2003) 2746–2750.
[48] E.A. Barringer, H.K. Bowen, Langmuir 1 (1985) 414–420.
[49] X. Liu, J. Yang, L. Wang, X. Yang, L. Lu, X. Wang, Mater. Sci. Eng. A 289 (2000) 241–245.
[50] Y. Xiang, P. Zhao, Z. Jin, B. Chen, H. Ming, H. Zhang, W. Zhang, G. Cao, X. Zhu, ACS Appl. Mater. Interfaces 10 (2018) 42258–42267.
[51] G. Wang, C. Lu, X. Zhang, B. Wan, H. Liu, M. Xia, H. Gou, G. Xin, J. Lian, Y. Zhang, Nanomater. Energy 36 (2017) 46–57.
[52] Y. Oh, S. Nam, S. Wi, J. Kang, T. Hwang, S. Lee, H.H. Park, J. Cabana, C. Kim, B. Park, J. Mater. Chem. 2 (2014) 2023–2027.
[53] J. Wang, Y. Zhou, Y. Hu, R. O'Hayre, Z. Shao, J. Phys. Chem. C 115 (2011) 2529–2536.
[54] J. Zhou, J. Qin, X. Zhang, C. Shi, E. Liu, J. Li, N. Zhao, C. He, ACS Nano 9 (2015) 3837–3848.
[55] C. Lin, X. Fan, Y. Xin, F. Cheng, M.O. Lai, H. Zhou, L. Lu, Nanoscale 6 (2014) 6651–6660.
[56] J. Ren, H. Ming, Z. Jia, Y. Zhang, J. Ming, Q. Zhou, J. Zheng, Energy Technol. 5 (2017) 1680–1686.
[57] X. Liu, S. Tong, C. Dai, P. He, H. Zhou, J. Solid State Electrochem. 19 (2015) 299–305.
[58] L. Gao, R. Liu, H. Hu, G. Li, Y. Yu, Nanotechnology 25 (2014) 175402.
[59] L. Wen, Z. Wu, H. Luo, R. Song, F. Li, J. Electrochem. Soc. 162 (2015) A3038–A3044.
[60] Y. Tang, L. Liu, H. Zhao, D. Jia, W. Liu, J. Mater. Chem. 4 (2016) 2089–2095.
[61] V. Augustyn, J. Come, M.A. Lowe, J.W. Kim, P.L. Taberna, S.H. Tolbert, H.D. Abruna, P. Simon, B. Dunn, Nat. Mater. 12 (2013) 518–522.
[62] Y. Yang, B. Qiao, X. Yang, L. Fang, C. Pan, W. Song, H. Hou, X. Ji, Adv. Funct. Mater. 24 (2014) 4349–4356.
[63] D. Wang, Z. Shan, R. Na, W. Huang, J. Tian, J. Power Sources 337 (2017) 11–17.
[64] X. Wang, H. Hao, J. Liu, T. Huang, A. Yu, Electrochim. Acta 56 (2011) 4065–4069.
[65] C. Wang, S. Wang, L. Tang, Y.-B. He, L. Gan, J. Li, H. Du, B. Li, Z. Lin, F. Kang, Nanomater. Energy 21 (2016) 133–144.
[66] J. Huang, H. Liu, N. Zhou, K. An, Y.S. Meng, J. Luo, ACS Appl. Mater. Interfaces 9 (2017) 36745–36754.